Supporting Information for

Atmospheric OH Oxidation Chemistry of Particulate Liquid Crystal Monomers: An Emerging Persistent Organic Pollutant in Air

Qifan Liu, John Liggio,* Jeremy Wentzell, Patrick Lee, Kun Li,# and Shao-Meng Li

Air Quality Processes Research Section, Environment and Climate Change Canada, Toronto, Ontario M3H 5T4, Canada

now at: Laboratory of Atmospheric Chemistry, Paul Scherrer Institute (PSI), 5232 Villigen, Switzerland

*Corresponding author.

Phone: 1-416-739-4840; e-mail: John. Liggio@canada.ca.

(20 Pages, 6 Figures, 3 Tables)

Contents

S1. Experimental details: Page S2

S2. Comparison of the EESI-TOFMS signal intensities of oxidation products of LCMs at different OH exposures: Page S4

S3. HR-TOF-AMS measurments: Page S5

S4. Other aspects of photooxidation mechanism of LCMs: Page S6

S5. Assessing the number of LCMs with long-range atmospheric transport potential: Page S7

Figures

S1: Signal intensity fractions for molecular ions of LCMs as a function of OH exposure.

S2: Proposed mechanism for the formation of products E_{33}–E_{40} during heterogeneous OH oxidation of particulate EPPB.

S3: Proposed mechanism for the heterogeneous OH oxidation of particulate EFPT.

S4: EESI-TOFMS signal intensities of the oxidation products of LCMs at different OH exposures.

S5: The differential HR-TOF-AMS spectra of unreacted and oxidized LCMs.

S6: Possible chemical structures for LCMs fragments measured by the HR-TOF-AMS.

Tables

S1: Physiochemical properties of EPPB and EFPT.

S2: Identified particulate products from the EESI-TOFMS in the heterogeneous OH oxidation of EPPB experiments.

S3: Identified particulate products from the EESI-TOFMS in the heterogeneous OH oxidation of EFPT experiments.

S1. Experimental details

S1.1 Reagents

1-ethyl-4-(4-(4-propylcyclohexyl)phenyl)benzene (EPPB; #E1162) and 4''-ethyl-2'-fluoro-4-propyl-1,1':4',1''-terphenyl (EFPT; #E1264) were purchased from TCI Chemicals. Ammonium sulfate (#A4915), sodium iodide (#383112), and acetonitrile (#50387) were purchased from Sigma-Aldrich. CO gas (0.1% in air) was purchased from Air Liquide. O_3 was produced by an O_3 generator (Ozone Solutions, model TG-10) supplied with high grade O_2 (Air Liquide, 99.999%).

S1.2 Photochemical oxidation flow reactor (OFR)

The total flow rate through the OFR was 0.9 L min^{-1} with a residence time of 60 s. The temperature of the reactor was maintained at 298 K by circulating water through an outer jacket of the reactor. The $(NH_4)_2SO_4$ particles (mode mobility diameter 73 nm) were generated via atomization (TSI, model 3706), dried through a diffusion drier (TSI, model 3062), and then passed through the headspace of a temperature-controlled Pyrex tube (343 K) containing a pure LCM, to generate coated particles with a calculated coating thickness of 3 nm (calculated based upon the shift in the peak of the particle size distribution). Upon achieving a steady-state concentration of LCM (15 μg m^{-3}) under 254 nm UV light irradiation (Jelight, #82-3309-9), O_3 (0–2 ppm) was introduced into the OFR. The RH in the OFR was constantly maintained at 35% by controlling the flow of dry and wet zero air into the OFR. The UV lamp inside the reactor was surrounded by a quartz sheath tube, which was purged with compressed air to cool the lamp. The O_3 concentration, RH, particle size distribution, and particulate LCM concentration were measured with an O_3 monitor (2B Technology, model 202), a RH sensor (Vaisala Inc., model HMP60), a scanning mobility particle sizer (SMPS, TSI), and an Aerodyne HR-TOF-AMS,[1] respectively. Control experiments demonstrated that O_3 had no effect on the degradation of LCMs. The particle-phase concentration of LCMs decreased <3% when exposed to 254 nm UV light in the absence of O_3, suggesting that the direct photolysis had negligible impacts on the degradation of LCMs.

Based on the estimated vapor pressure of EPPB and EFPT (< 10^{-4} Pa; see Table S1),[2] these two LCMs are considered to be non-volatile and should mainly remain in the particle-phase (rather than gas-phase) during the OFR experiments. To further verify this hypothesis, the LCMs coated on $(NH_4)_2SO_4$ particles were introduced into the OFR after having passed through an activated carbon denuder which can remove volatile organics vapors from the flow. It was found that the size distribution of the coated particles (measured using a SMPS) remained unchanged after passing through the denuder. In addition, if a large fraction of LCMs were present in the gas-phase, they would likely form secondary organic materials upon OH oxidation, thus resulting in an enhancement in the mass concentration of the total particulate organics. However, this is not the case for these two LCMs. The mass concentration of the total particulate organics remained stable during the OH oxidation experiments, as measured by the HR-TOF-AMS. Together, these results suggest that the two LCMs studied here are non-volatile and mainly remain in the particle-phase during the OFR experiments, and are subjected to OH heterogeneous oxidation only.

In the atmosphere, gas-phase OH radicals can react with particulate LCMs through two pathways: gas-particle surface reactions and particle-phase reactions (OH diffuses into a particle and reacts with a LCM). Here, the derived effective rate constant (k_{eff}) considers the whole heterogeneous process which includes both pathways, and thus is relevant to the atmospheric processing of particulate LCMs and can be used to estimate the atmospheric persistence of LCMs.

S1.3 EESI-TOFMS

The particulate products formed from the heterogeneous OH oxidation of LCMs were measured using an EESI-TOFMS which had been described previously.[3,4] The sample flow was introduced into the EESI-TOFMS, either directly or through a particle filter to provide a background measurement. During the experiments, 20–30 mins of LCM particle sampling was alternated with 3–5 mins through the filter. The sample flow also passed through a multi-channel extruded carbon denuder (length 5cm, outer diameter 6mm) housed in a stainless steel tube which removed most trace gas-phase species with high efficiency (e.g., >99.6% for pinonic acid).[3] The aerosol particles collide with the electrospray droplets generated at the end of a commercially available electrospray capillary (length 50 cm; inner diameter 50 µm; outer diameter 360 µm; New Objective; #TT360-50-50-N-5) at a flow rate of 1 µL min^{-1}. The soluble components of the particle were extracted, ionized via a Coulombic explosion of the charged droplets, and detected by a Tofwerk APi-TOFMS (resolution ~5500 at *m*/*z* 329). The sample flow remained unheated until after the extraction process, thus minimizing the volatilization and thermal decomposition of the labile particle-phase components. The extracted droplets then entered the APi-TOFMS through a capillary tube (length 70 mm; inner diameter 0.5mm; outer diameter 1.6 mm) heated to 523 K to ensure that these droplets evaporated during the transit through the capillary tube. It should be noted that, given the short residence time in this capillary (~1 ms), the effective temperature experienced by the analyzer was much lower than 523 K and no thermal decomposition was observed.[4] The electrospray working solution was a CH_3CN–H_2O mixture (80:20 by volume) with 200 ppm of NaI as a charge carrier. The potential difference between the ESI probe and APi-TOFMS was set to +2.5 kV. As a result, the mass spectra were recorded in positive ion mode (i.e., Na^+ adducts). A series of $[(NaI)_x(CH_3CN)_y(H_2O)_z]Na^+$ clusters (x=0–3, y=0–2, z=0–2) which ranged from *m*/*z* 23 to 491 were utilized for *m*/*z* calibration.[5] In Figure 1, these $[(NaI)_x(CH_3CN)_y(H_2O)_z]Na^+$ clusters are removed because the difference of two high intensity signals would remain large relative to most ions in the mass spectra.

As shown in Figure 1A, for the EPPB molecule and its oxidation products, the abundances of $[M(CH_3CN)]Na^+$ clusters are 35–60% of the parent ion ($[M+Na^+]$). For the EFPT molecule and its oxidation products, the abundance ratios of $[M(CH_3CN)]Na^+$ to $[M+Na^+]$ clusters are in the range of 25–48% (Figure 1B). A previous study has shown that the abundance of $[M(CH_3CN)]Na^+$ is on the order of 10% of $[M+Na^+]$ (M= α-pinene SOA components).[3] The higher abundance of $[M(CH_3CN)]Na^+$ clusters observed here (relative to the previous study) is attributed to the higher CH_3CN content used in the current electrospray working solution (80% by volume; previously 50% by volume). Regardless, the current and

previous results[3] suggest that organic molecules can form both $[M+Na^+]$ and $[M(CH_3CN)]Na^+$ clusters during the EESI-TOFMS measurements, with a higher abundance for the former cluster.

S1.4 OH exposure measurement

The OH exposure (molecules cm^{-3} s), which is the product of OH concentration (molecules cm^{-3}) and residence time (s) in the reactor, was determined by measuring the loss of CO as a function of O_3 concentration in offline calibrations:

$$\text{OH exposure} = -\frac{1}{k_{\text{CO}}} \ln \frac{[\text{CO}]_\text{t}}{[\text{CO}]_0}$$

where k_{CO} is the second-order rate constant of CO at 298 K (1.54×10^{-13} cm^3 $molecules^{-1}$ s^{-1}),[6] $[CO]_t$ is the CO concentration measured by a CO monitor (LGR, model 23r) in the presence of O_3, $[CO]_0$ (1.5 ppm) is the measured CO concentration in the absence of O_3. The measured OH exposures ranged from 4.7×10^{10} to 1.6×10^{12} molecules cm^{-3} s.

S2. Comparison of the EESI-TOFMS signal intensities of the oxidation products of LCMs at different OH exposures

As shown in Figure S4A, the EESI-TOFMS signal intensities of most oxidation products (80% of the total products) of EPPB increased with an increase of OH exposure from 2.6×10^{11} to 6.1×10^{11} molecules cm^{-3} s. It is interesting to note that the relative signal enhancements for early-generation products (first and second-generation products) with increased OH exposure were generally more prominent than those of later-generation products (third and fourth-generation products). For example, the signal intensities of products E_1–E_3 (first and second-generation products) increased by up to 116% with increased OH exposure, whereas products E_4–E_5 (third and fourth-generation products) had a relatively lower signal enhancement (22–50%) as shown in the inset graph A2 in Figure S4A. A higher signal enhancement for early-generation products can be expected as only a portion of these products can be converted to various later-generation products during OH oxidation. This is consistent with a previous study on particulate succinic acid ($C_4H_6O_4$) which similarly demonstrated that the relative signal enhancement for early-generation photooxidation product malic acid ($C_4H_6O_5$) with increased OH exposure is more prominent than later-generation products such as tartaric acid ($C_4H_6O_6$) and 2-hydroxy-3-oxosuccinic acid ($C_4H_4O_6$).[7] The observations outlined here further confirms the validity of currently proposed oxidation mechanism for EPPB.

We also note that the signal intensities of products E_{14}–E_{16}, and E_{29} exhibited an opposite trend, i.e., their signal intensities decreased with increased OH exposure, as shown in the inset graph A1 in FigureS4A. Given that all of these four compounds have at least one hydroperoxide functional group (OOH; see Figure 2A), the observed signal intensity reduction here are likely related to the peroxide chemistry. It's well-known that OH exposure has complex impacts (formation vs. decomposition) on the peroxide chemistry.[8-10] With increased OH exposure, more EPPB molecules would be consumed, producing more

oxidation products, including peroxides. On the other hand, peroxides are known to be very reactive,[11-13] and serve as key reaction intermediates during OH oxidation of EPPB (Figure 2A), which can be converted to other non-peroxide products such as carbonyls, alcohols, and carboxyl acids with continued OH oxidation. Thus, if the peroxide decomposition process dominated over the formation pathway, we would see a decreased peroxide content, as was the case for products E_{14}–E_{16}, and E_{29}. However, in the case of other formed peroxides (e.g., products E_1 and E_6), their signal intensities were observed to increase with increased OH exposure, suggesting that the peroxide formation pathway dominated over the decomposition process for these compounds. Therefore, for the peroxide products, the interplay between these two opposite effects (formation vs. decomposition) depends on the chemical reactivities, the reaction pathways, and OH exposures.

Similarly, in the case of EFPT, the signal intensities of most formed products (80% of the total products) increased with increased OH exposure (Figure S4B), with a generally higher relative signal enhancement for early-generation products relative to later-generation products (see the inset figure in Figure S4B). The signal intensity of product F_1 (a peroxide) decreased with increased OH exposure. Overall, the experimental results here reflect a complex peroxide evolution during photooxidation of LCMs, and further study is warranted to gain insights into the peroxide chemistry.

S3. HR-TOF-AMS measurements

S3.1 Assessing the impact of fragmentation of oxidation products on the selected tracer ions of LCMs

As mentioned in the main text, the molecular-ion peaks at *m*/*z* 306 and *m*/*z* 318 were selected as tracer ions for EPPB and EFPT, respectively. In theory, during heterogeneous OH oxidation, the fragments of some oxidation products (molecular-ions greater than a selected tracer ion) may lead to an interference in the signal of a tracer ion. However, this interference is likely to be negligible for the two LCMs investigated here, as discussed below. As shown in Table S2 and S3, all of the oxidation products have at least one oxygenated functional group (OOH, OH, C=O, and COOH). Based on the known fragmentation pathways of such compounds (ROOH, ROH, RCHO, and RCOOH),[14] the most prominent fragment should be $[M–OOH]^+$, $[M–OH]^+$ or $[M–CH_2OH]^+$, $[M–CO]^+$, and $[M–CO_2]^+$, respectively. However, none of these fragments have the same *m*/*z* ions with the selected tracer ions. Further, as shown in the differential HR-TOF-AMS spectra between the oxidized and unreacted LCMs (Figure S5), no significant fragments were observed for the *m*/*z* ions greater than the molecular-ions of the parent LCMs. Together, these results clearly suggest that the oxidation products and their subsequent smaller *m*/*z* fragments have negligible impacts on the selected tracer ions.

S3.2 Chemical degradation of LCMs

The chemical degradation of particulate LCMs can be observed from the HR-TOF-AMS measurements during a given experiment. The differential aerosol mass spectra between the oxidized and unreacted LCMs (oxidized−unreacted) are shown in Figure S5.

When particulate EPPB was exposed to OH radicals, a decrease in the signals at *m*/*z* channels 306, 291, 221, 208, 193, 178, 165, 81, 75, 55, and 41, was observed (Figure S5A). These mass peaks correspond to $C_{23}H_{30}^{+}$, $C_{22}H_{27}^{+}$, $C_{17}H_{17}^{+}$, $C_{16}H_{16}^{+}$, $C_{15}H_{13}^{+}$, $C_{14}H_{10}^{+}$, $C_{13}H_{9}^{+}$, $C_{6}H_{9}^{+}$, $C_{6}H_{3}^{+}$, $C_{4}H_{7}^{+}$, and $C_{3}H_{5}^{+}$ respectively, while *m*/*z* 306 represents the molecular ion of EPPB. The likely chemical structures for these fragments are given in Figure S6A. The decrease of above mass peaks upon OH exposure indicated that the degradation of EPPB occurred. Conversely, fragments at *m*/*z* 322, 147, 73, and 44 increased due to the presence of oxidation products and their associated fragmentation, i.e., $C_{23}H_{30}O^{+}$ (*m*/*z* 322), $C_{6}H_{11}O_{4}^{+}$ (*m*/*z* 147), $C_{4}H_{9}O^{+}$ (*m*/*z* 73), and CO_{2}^{+} (*m*/*z* 44). The fragment at *m*/*z* 322 may be the molecular ion of product E_{17} in Figure 2A, and is indicative of OH-addition to the phenyl ring during heterogeneous OH oxidation EPPB, consistent with the chemical mechanism of OH oxidation of benzene[15] and with the molecular products observed with the EESI-TOFMS.

In the case of EFPT, a decrease of mass peaks at *m*/*z* 318, 303, 289, 274, 183, and 137 was observed with OH exposure (Figure S5B). These mass peaks correspond to $C_{23}H_{23}F^{+}$, $C_{22}H_{20}F^{+}$, $C_{21}H_{18}F^{+}$, $C_{20}H_{15}F^{+}$, $C_{13}H_{8}F^{+}$, and $C_{9}H_{10}F^{+}$ respectively, while *m*/*z* 318 represents the molecular ion of EFPT. The likely chemical structures for these fragments are given in Figure S6B. Concurrently, oxidation of EFPT resulted in the appearance of several oxygenated fragments at *m*/*z* 147, 73, and 44, corresponding to $C_{6}H_{11}O_{4}^{+}$, $C_{4}H_{9}O^{+}$, and CO_{2}^{+}, respectively.

Together, the HR-TOF-AMS measurement results presented here suggest that the HR-TOF-AMS can provide only limited information for the oxidation products of LCMs, which can be mitigated through the use of the EESI-TOFMS.

S4. Other aspects of photooxidation mechanism of LCMs

As mentioned in the main text, OH radicals can attack various carbon atoms of the alkyl, phenyl, and cyclohexyl groups of LCMs. The probability of the three different reaction pathways are likely different. It is well known that different organic molecules have different reactivities towards OH, depending upon their chemical structures which will be reflected in their associated kinetics.[16] The measured rate constants of ethane, propane, benzene, fluorobenzene, and cyclohexane with OH are 2.48×10^{-13}, 1.09×10^{-12}, 1.22×10^{-12}, 8.70×10^{-13}, and 6.97×10^{-12} molecule^{-1} cm^{3} s^{-1}, respectively.[16,17] Given the above kinetics, the relative importance of OH reaction sites in EPPB may follow the sequence: cyclohexyl > phenyl > propyl > ethyl group; whereas for EFPT the likely sequence is: phenyl > propyl > fluorophenyl > ethyl group. Consequently, this may be manifested in the relative importance of various oxidation products presented in Figure 2A and Figure S3.

S5. Assessing the number of LCMs with long-range atmospheric transport potential

A previous study suggested that while the AOPWIN model cannot provide reliable kinetic data for compounds beyond its application domain, it may provide a reliable relative trend. We note that this is also true for the currently investigated LCMs. For example, as shown in Table 1, the AOPWIN predicted rate constant for EPPB is ~2 times higher than that of EFPT and a similar trend also holds for the measured heterogeneous rate constants (heterogeneous k_{EPPB} is ~1.5 times higher than k_{EFPT}). This suggests that if compound A and compound B have similar structures and A has a higher AOPWIN predicted rate constant than B, then A will likely have a higher heterogeneous rate constant than B. Following this logic, if a LCM has a similar or lower AOPWIN predicted rate constant compared to EPPB, it likely has a similar or longer atmospheric persistence compared to EPPB. Among the 362 currently produced LCMs,[2] ~190 LCMs have a similar or lower AOPWIN predicted rate constant compared to EPPB. As a result, these 190 LCMs may have the potential to undergo long-range atmospheric transport. More research is needed to investigate the atmospheric transformations of these LCMs.

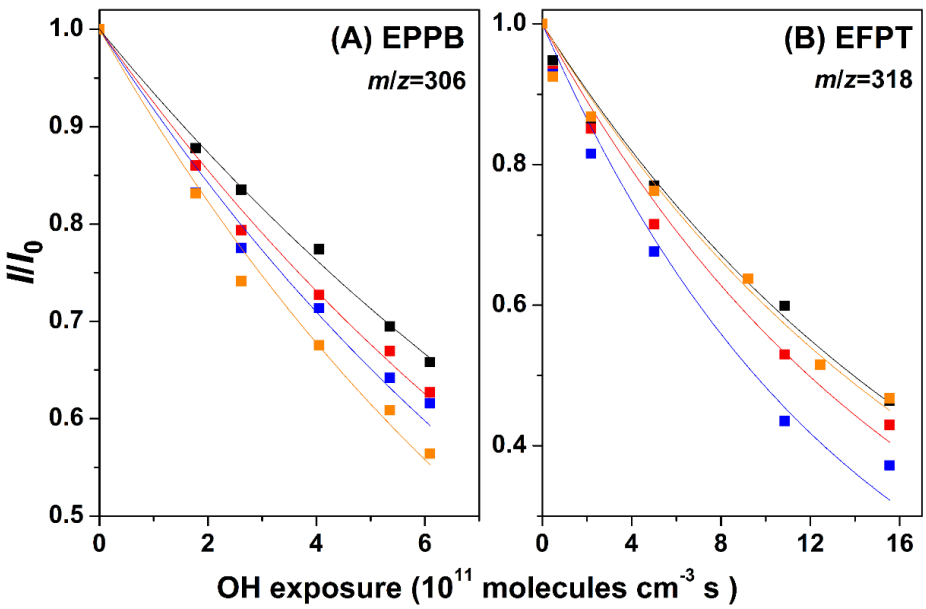

Figure S1. Signal intensity fractions for molecular ions of (**A**) EPPB and (**B**) EFPT coated on $(NH_4)_2SO_4$ as a function of OH exposure at 298 K and 35% RH (measured using a HR-TOF-AMS). The color series indicate independent experiments.

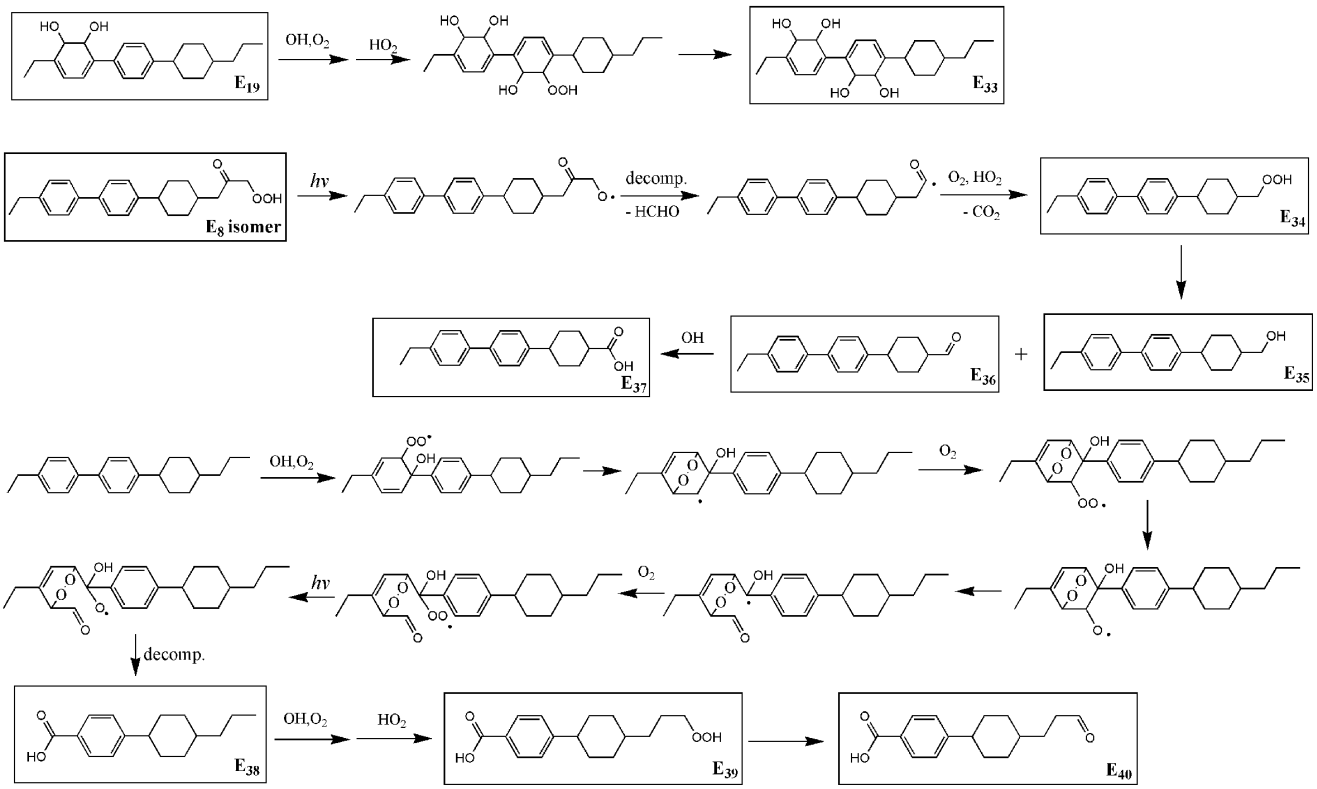

Figure S2. Proposed mechanism for the formation of products E_{33}–E_{40} during heterogeneous OH oxidation of particulate EPPB. The particulate products specifically measured by the EESI-TOFMS are indicated by the black boxes.

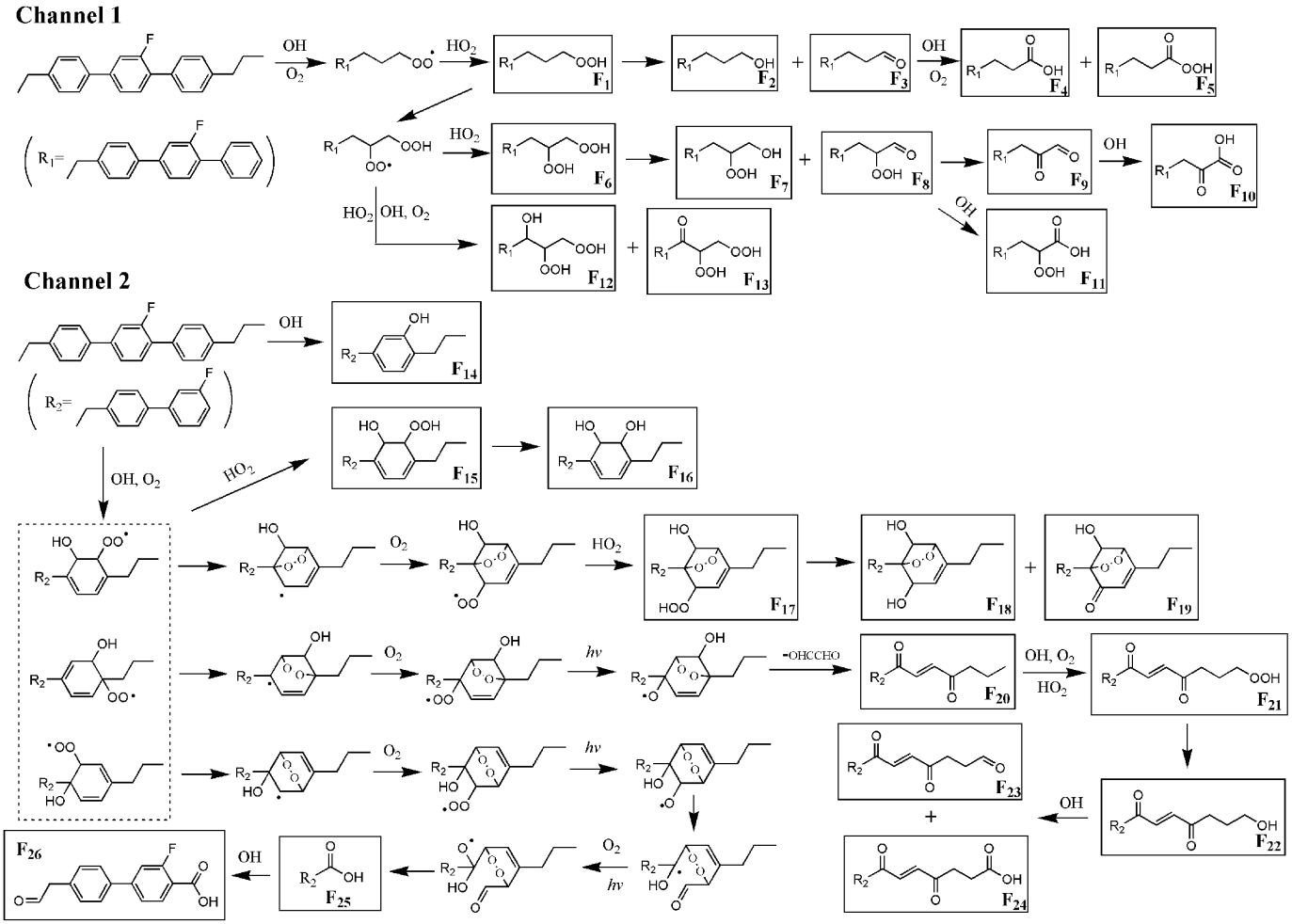

Figure S3. Proposed mechanism for the heterogeneous OH oxidation of particulate EFPT. The particulate products specifically measured by the EESI-TOFMS are indicated by the solid black boxes.

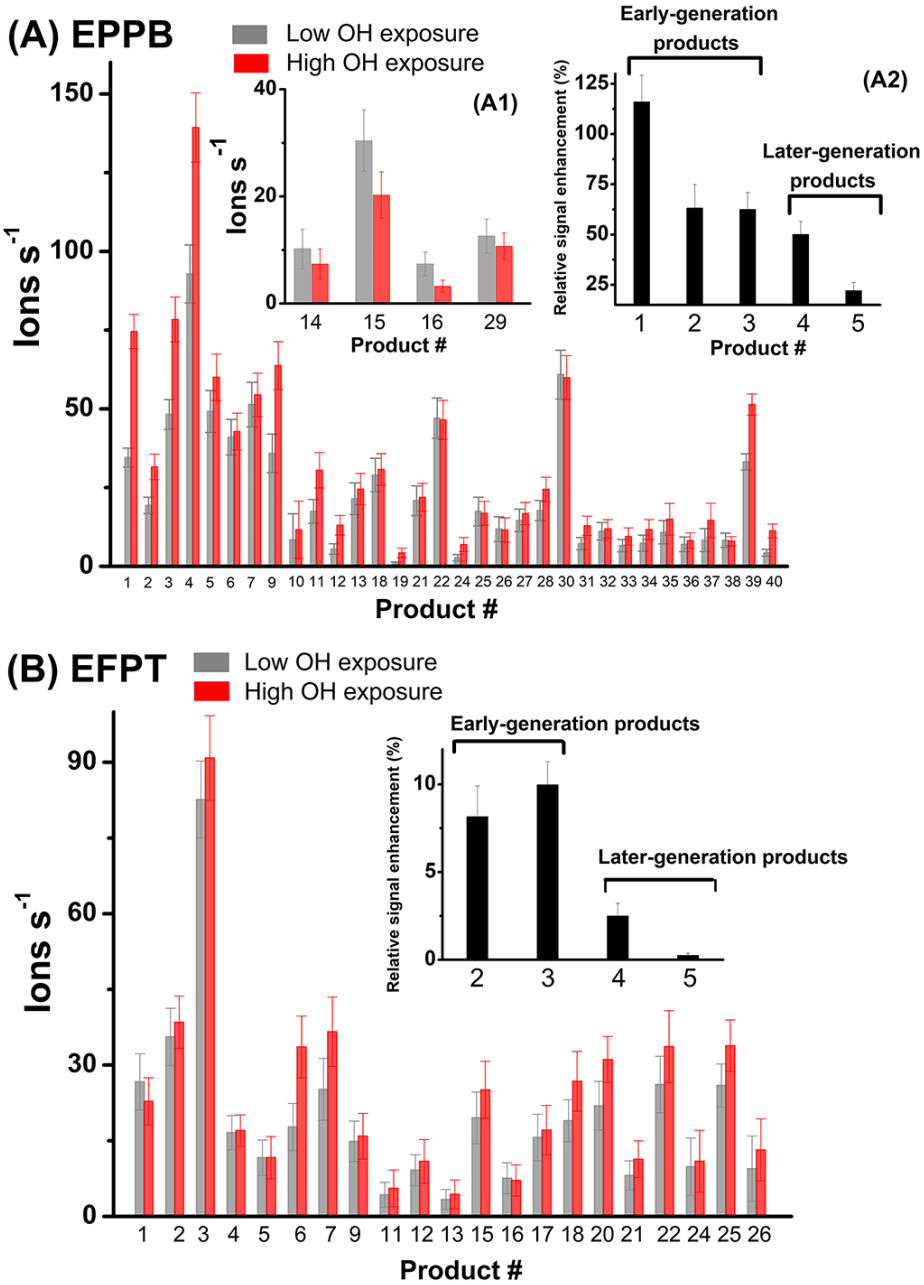

Figure S4. (**A**) EESI-TOFMS signal intensities of the oxidation products of EPPB at low (2.6×10^{11} molecules cm^{-3} s) and high OH exposures (6.1×10^{11} molecules cm^{-3} s). The inset graph A1 shows the signal intensities of products E_{14}–E_{16}, and E_{29}. The inset graph A2 shows the relative signal enhancement (%) for products E_1–E_5. The relative signal enhancement (%) = (the signal intensity of a given product at high OH exposure/ the signal intensity at low OH exposure – 1)×100%. (**B**) EESI-TOFMS signal intensities of the oxidation products of EFPT at low (1.1×10^{12} molecules cm^{-3} s) and high OH exposures (1.6×10^{12} molecules cm^{-3} s). The inset graph in part B shows the relative signal enhancement (%) for products F_2–F_5. All compound numbers refer to product molecules as labelled in Table S2 and S3.

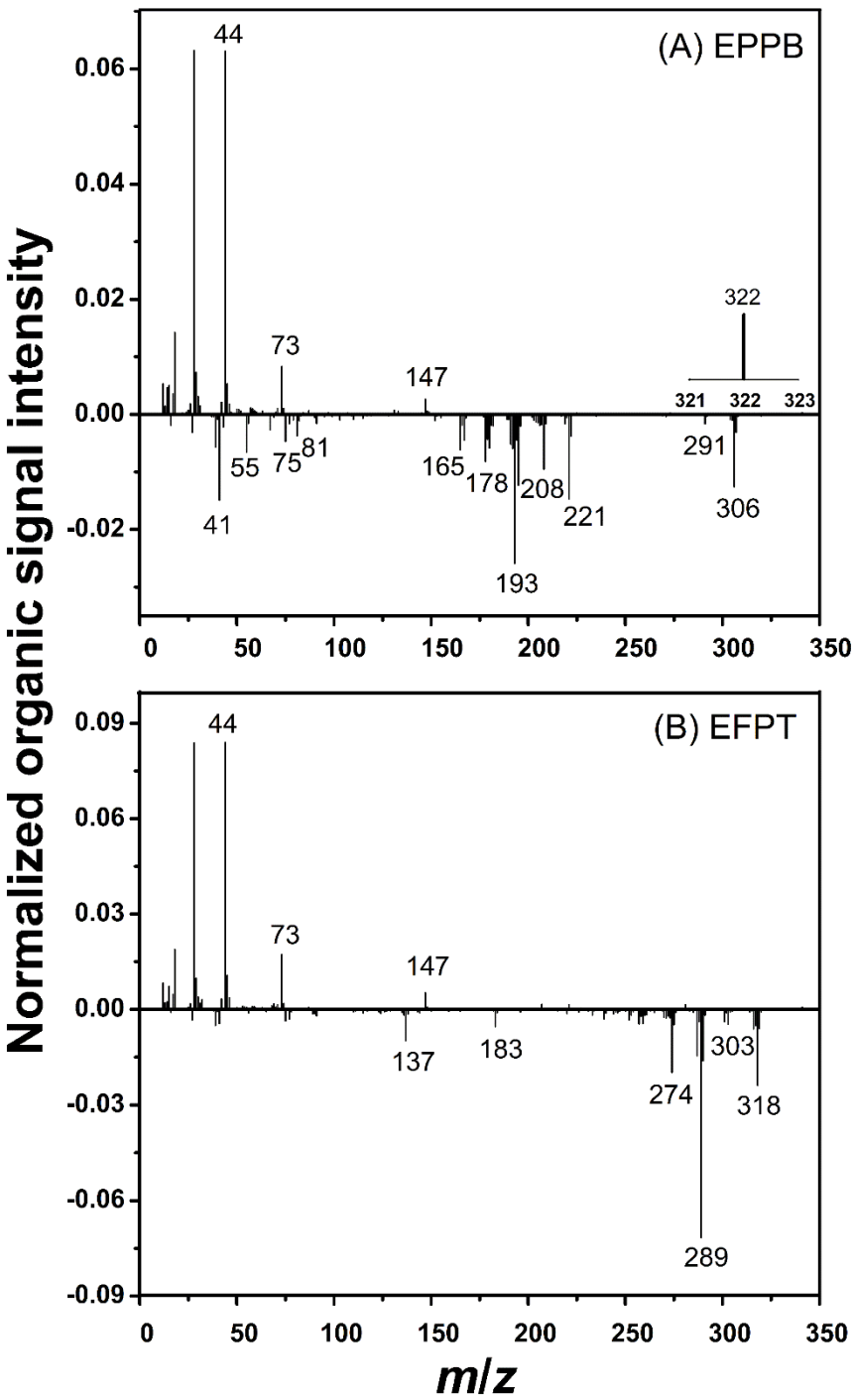

Figure S5. The differential aerosol spectra for LCMs (oxidized−unreacted) as measured by the HR-TOF-AMS: (A) EPPB at an OH exposure of 6.1×10^{11} molecules cm^{-3} s; (B) EFPT at an OH exposure of 1.6×10^{12} molecules cm^{-3} s. Positive and negative values indicate the mass fragments that are enhanced and reduced for LCMs upon OH exposure, respectively. The inset graph in part A shows the corresponding magnified area.

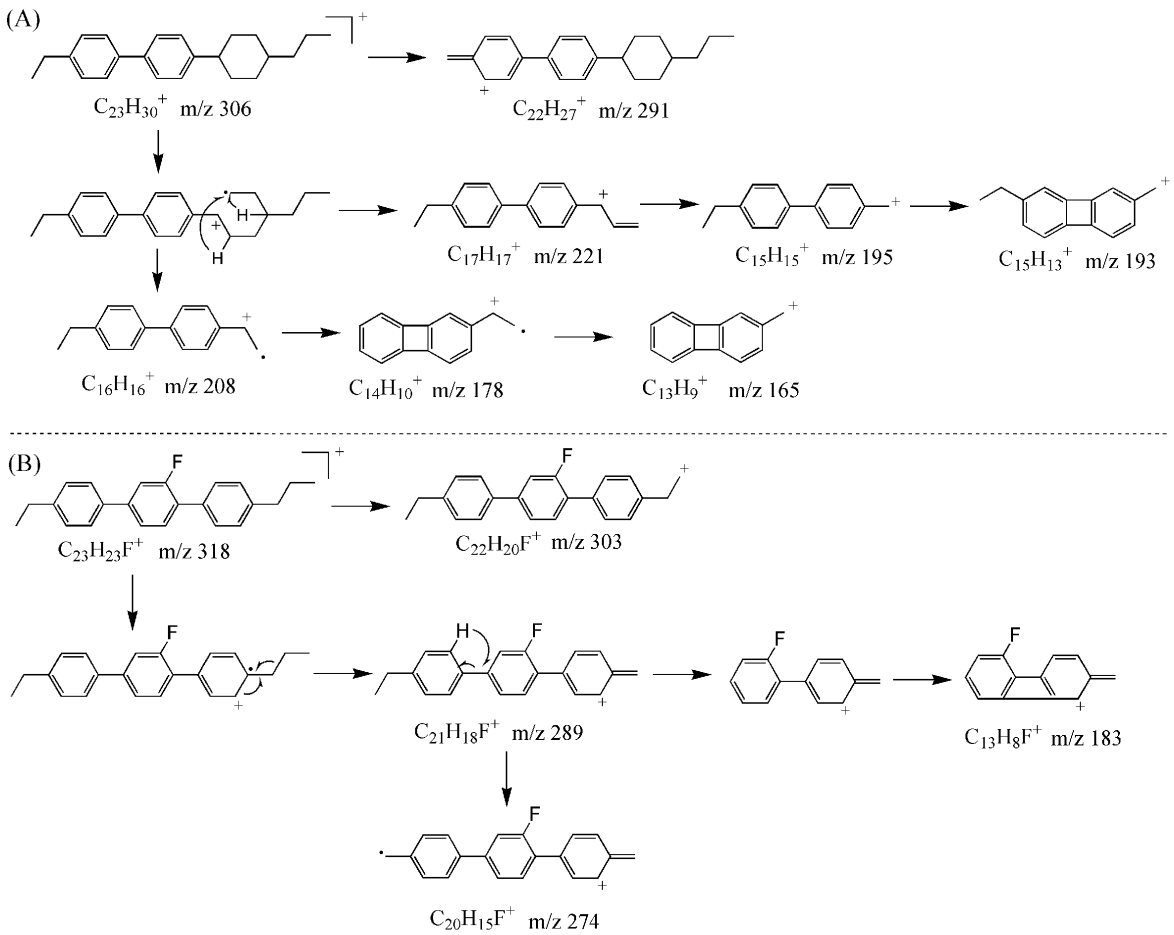

Figure S6. Possible chemical structures for (**A**) EPPB and (**B**) EFPT fragments measured by the HR-TOF-AMS.[2]

Table S1. Physiochemical properties of EPPB and EFPT.[2]

Chemical name	Abbreviation	Chemical structure	Molecular weight (g mol^{-1})	Estimated vapor pressure ($\times 10^{-5}$ Pa)	BCF[a]
1-ethyl-4-(4-(4-propylcyclohexyl)phenyl)benzene	EPPB	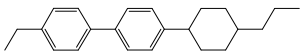	306.23	3.24	1374
4''-ethyl-2'-fluoro-4-propyl-1,1':4',1''-terphenyl	EFPT	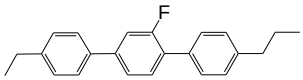	318.18	0.48	3105

[a] BCF: bioaccumulation potential; BCF>1000 indicates that after entering into the environment, these two LCMs have potential for bioaccumulation.

Table S2. Identified particulate products from EESI-TOFMS in the heterogeneous OH oxidation of EPPB experiments.[a]

Product ID	Chemical formula	Molecular weight	M+Na	Proposed chemical structure
E_1	$C_{23}H_{30}O_2$	338.22	361.21	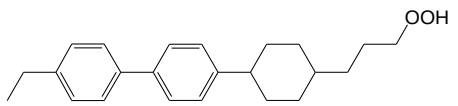
E_2	$C_{23}H_{30}O$	322.23	345.22	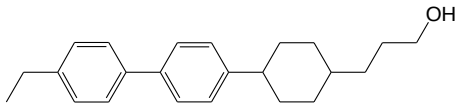
E_3	$C_{23}H_{28}O$	320.21	343.20	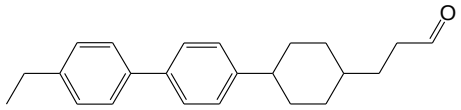
E_4	$C_{23}H_{28}O_2$	336.21	359.20	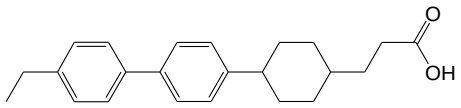
E_5	$C_{23}H_{28}O_3$	352.20	375.19	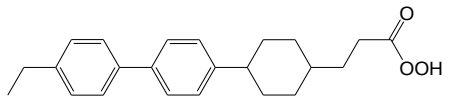
E_6	$C_{23}H_{30}O_4$	370.21	393.20	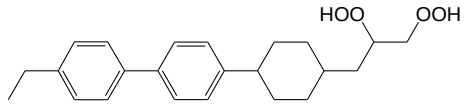
E_7	$C_{23}H_{30}O_3$	354.22	377.21	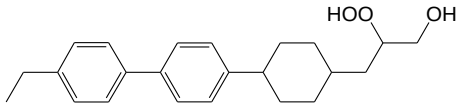
E_8	$C_{23}H_{28}O_3$	352.20	375.19	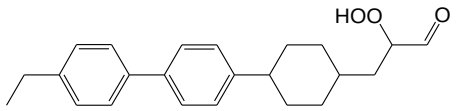
E_9	$C_{23}H_{26}O_2$	334.19	357.18	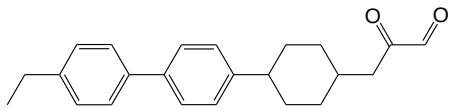
E_{10}	$C_{23}H_{26}O_4$	366.18	389.17	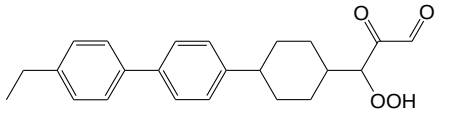

E_{11}	$C_{23}H_{26}O_3$	350.19	373.18	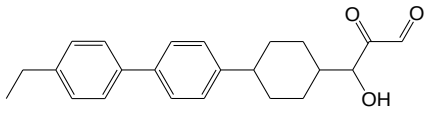
E_{12}	$C_{23}H_{24}O_3$	348.17	371.16	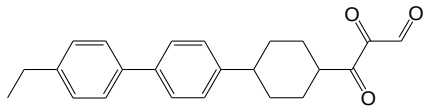
E_{13}	$C_{23}H_{28}O_4$	368.20	391.19	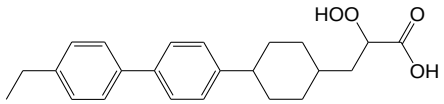
E_{14}	$C_{23}H_{30}O_6$	402.20	425.19	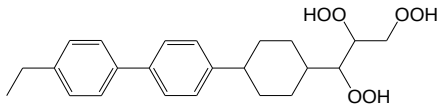
E_{15}	$C_{23}H_{30}O_5$	386.21	409.20	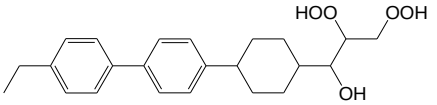
E_{16}	$C_{23}H_{28}O_5$	384.19	407.18	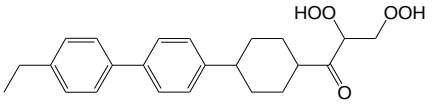
E_{17}	$C_{23}H_{30}O$	322.23	345.22	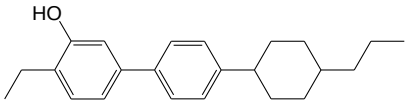
E_{18}	$C_{23}H_{32}O_3$	356.23	379.22	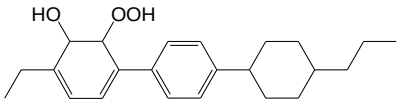
E_{19}	$C_{23}H_{32}O_2$	340.24	363.23	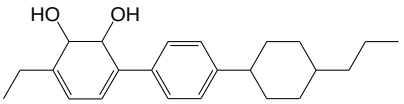
E_{20}	$C_{23}H_{30}O_2$	338.22	361.21	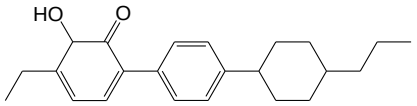
E_{21}	$C_{23}H_{32}O_5$	388.22	411.21	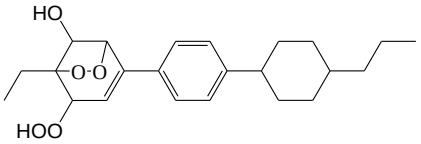

E_{22}	$C_{23}H_{32}O_4$	372.23	395.22	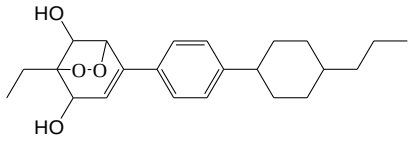
E_{23}	$C_{23}H_{30}O_4$	370.21	393.20	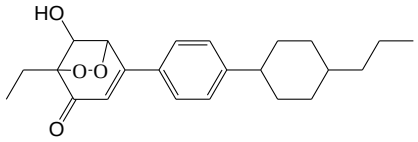
E_{24}	$C_{19}H_{24}O_2$	284.18	307.17	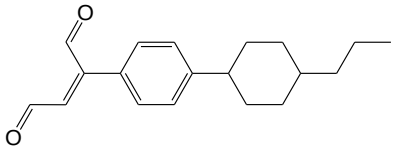
E_{25}	$C_{19}H_{24}O_3$	300.17	323.16	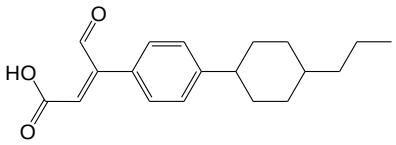
E_{26}	$C_{19}H_{24}O_4$	316.17	339.16	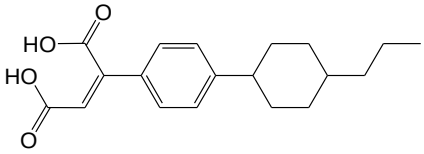
E_{27}	$C_{18}H_{24}O_3$	288.17	311.16	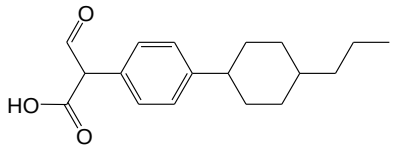
E_{28}	$C_{21}H_{28}O_2$	312.21	335.20	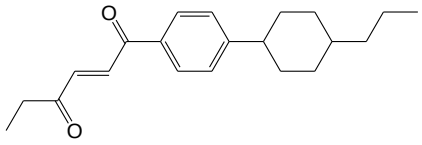
E_{29}	$C_{21}H_{28}O_4$	344.20	367.19	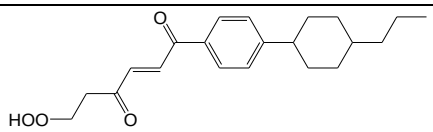
E_{30}	$C_{21}H_{28}O_3$	328.20	351.19	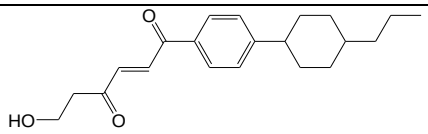
E_{31}	$C_{21}H_{26}O_3$	326.19	349.18	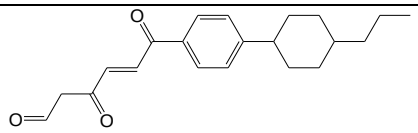

E_{32}	$C_{21}H_{26}O_4$	342.18	365.17	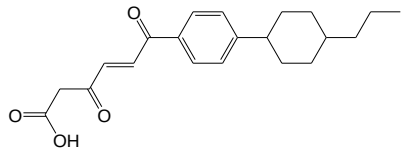
E_{33}	$C_{23}H_{34}O_4$	374.25	397.24	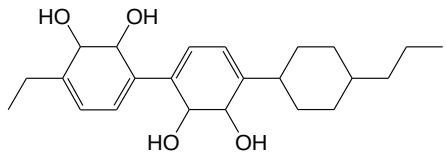
E_{34}	$C_{21}H_{26}O_2$	310.19	333.18	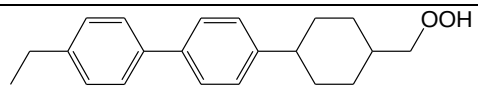
E_{35}	$C_{21}H_{26}O$	294.20	317.19	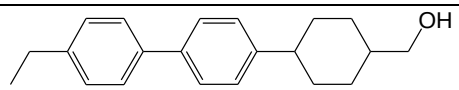
E_{36}	$C_{21}H_{24}O$	292.18	315.17	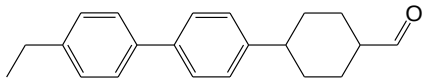
E_{37}	$C_{21}H_{24}O_2$	308.18	331.17	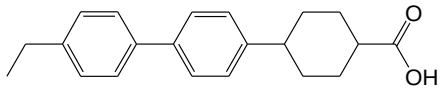
E_{38}	$C_{16}H_{22}O_2$	246.16	269.15	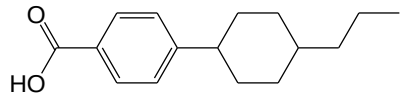
E_{39}	$C_{16}H_{22}O_4$	278.15	301.14	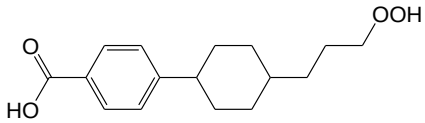
E_{40}	$C_{16}H_{20}O_3$	260.14	283.13	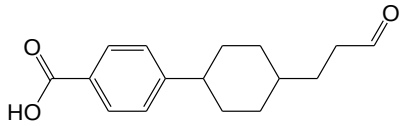

[a] Note products E_1 and E_{20} (*m*/*z* 361.21), E_2 and E_{17} (*m*/*z* 345.22), E_5 and E_8 (*m*/*z* 375.19), and E_6 and E_{23} (*m*/*z* 393.20), have the same molecular formula, and EESI-TOFMS is unable to distinguish such isomers from each other.

Table S3. Identified particulate products from EESI-TOFMS in the heterogeneous OH oxidation of EFPT experiments.[a]

Product ID	Chemical formula	Molecular weight	M+Na	Proposed chemical structure
F_1	$C_{23}H_{23}FO_2$	350.17	373.16	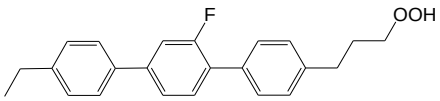
F_2	$C_{23}H_{23}FO$	334.17	357.16	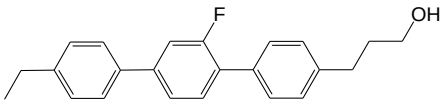
F_3	$C_{23}H_{21}FO$	332.16	355.15	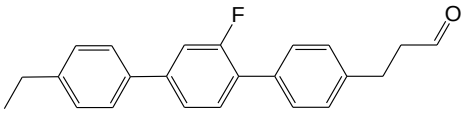
F_4	$C_{23}H_{21}FO_2$	348.15	371.14	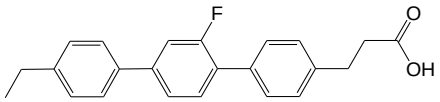
F_5	$C_{23}H_{21}FO_3$	364.15	387.14	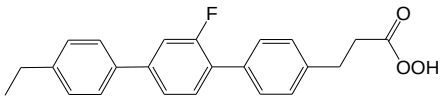
F_6	$C_{23}H_{23}FO_4$	382.16	405.15	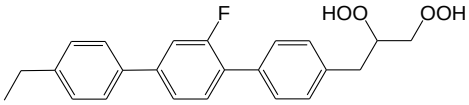
F_7	$C_{23}H_{23}FO_3$	366.16	389.15	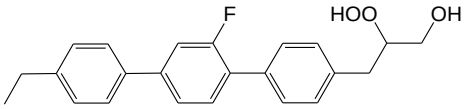
F_8	$C_{23}H_{21}FO_3$	364.15	387.14	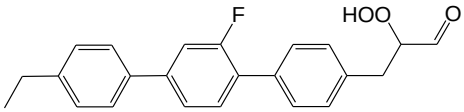
F_9	$C_{23}H_{19}FO_2$	346.14	369.13	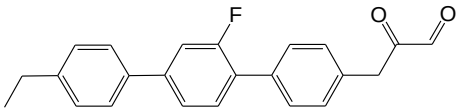
F_{10}	$C_{23}H_{19}FO_3$	362.13	385.12	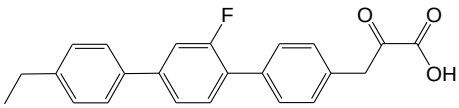

F_{11}	$C_{23}H_{21}FO_4$	380.14	403.13	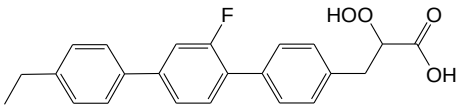
F_{12}	$C_{23}H_{23}FO_5$	398.15	421.14	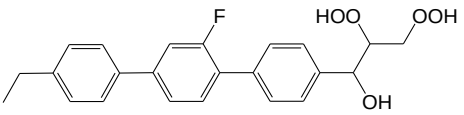
F_{13}	$C_{23}H_{21}FO_5$	396.14	419.13	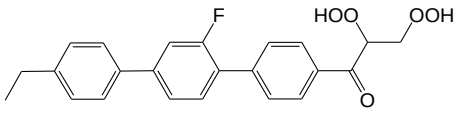
F_{14}	$C_{23}H_{23}FO$	334.17	357.16	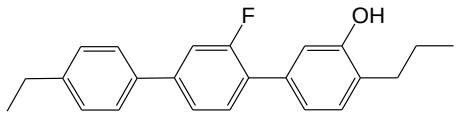
F_{15}	$C_{23}H_{25}FO_3$	368.18	391.17	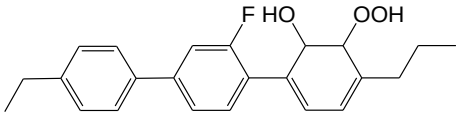
F_{16}	$C_{23}H_{25}FO_2$	352.18	375.17	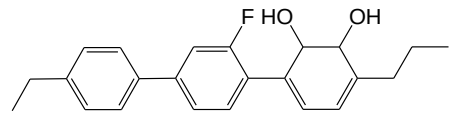
F_{17}	$C_{23}H_{25}FO_5$	400.17	423.16	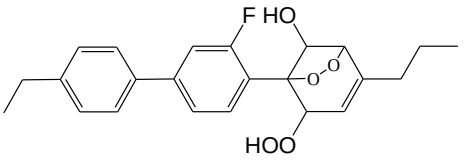
F_{18}	$C_{23}H_{25}FO_4$	384.17	407.16	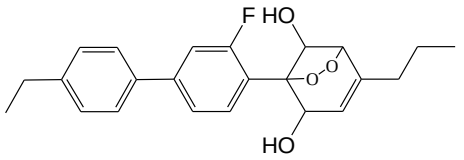
F_{19}	$C_{23}H_{23}FO_4$	382.16	405.15	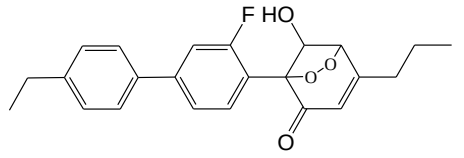
F_{20}	$C_{21}H_{21}FO_2$	324.15	347.14	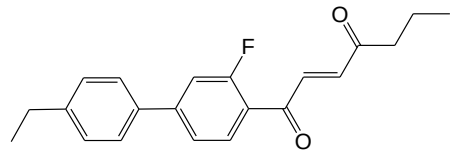

F_{21}	$C_{21}H_{21}FO_4$	356.14	379.13	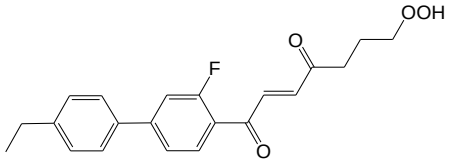
F_{22}	$C_{21}H_{21}FO_3$	340.15	363.14	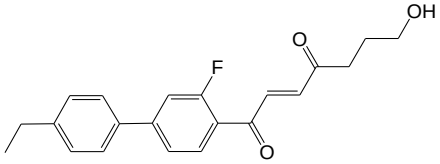
F_{23}	$C_{21}H_{19}FO_3$	338.13	361.12	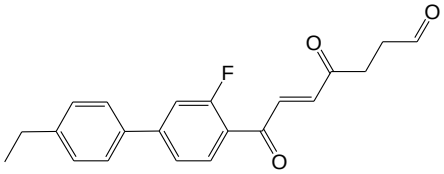
F_{24}	$C_{21}H_{19}FO_4$	354.13	377.12	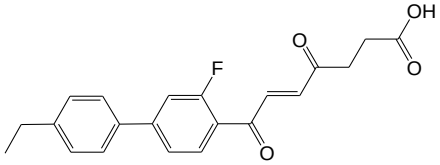
F_{25}	$C_{15}H_{13}FO_2$	244.09	267.08	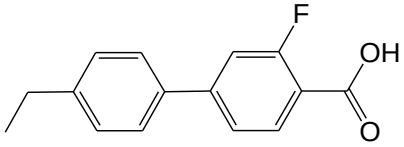
F_{26}	$C_{15}H_{11}FO_3$	258.07	281.06	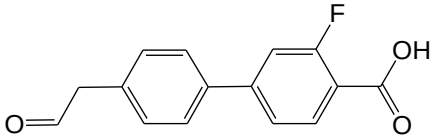

[a] Note products F_2 and F_{14} (*m*/*z* 357.16), F_5 and F_8 (*m*/*z* 387.14), and F_6 and F_{19} (*m*/*z* 405.15), have the same molecular formula, and EESI-TOFMS is unable to distinguish such isomers from each other.

References

(1) DeCarlo, P. F.; Kimmel, J. R.; Trimborn, A.; Northway, M. J.; Jayne, J. T.; Aiken, A. C.; Gonin, M.; Fuhrer, K.; Horvath, T.; Docherty, K. S.; Worsnop, D. R.; Jimenez, J. L. et al. Field-deployable, high-resolution, time-of-flight aerosol mass spectrometer. *Anal. Chem.* **2006,** *78*, 8281-8289.

(2) Su, H.; Shi, S.; Zhu, M.; Crump, D.; Letcher, R. J.; Giesy, J. P.; Su, G. Persistent, bioaccumulative, and toxic properties of liquid crystal monomers and their detection in indoor residential dust. *Proc. Natl. Acad. Sci. USA* **2019,** *116*, 26450-26458.

(3) Lopez-Hilfiker, F. D.; Pospisilova, V.; Huang, W.; Kalberer, M.; Mohr, C.; Stefenelli, G.; Thornton, J. A.; Baltensperger, U.; Prévôt, A. S. H.; Slowik, J. G. An extractive electrospray ionization time-of-flight mass spectrometer (EESI-TOF) for online measurement of atmospheric aerosol particles. *Atmos.*

Meas. Tech. **2019,** *12*, 4867-4886.
(4) Qi, L.; Chen, M.; Stefenelli, G.; Pospisilova, V.; Tong, Y.; Bertrand, A.; Hueglin, C.; Ge, X.; Baltensperger, U.; Prévôt, A. S. H.; Slowik, J. G. Organic aerosol source apportionment in Zurich using an extractive electrospray ionization time-of-flight mass spectrometer (EESI-TOF-MS)-Part 2: biomass burning influences in winter. *Atmos. Chem. Phys.* **2019,** *19*, 8037-8062.
(5) Liu, Q.; Liggio, J.; Wu, D.; Saini, A.; Halappanavar, S.; Wentzell, J. J.; Harner, T.; Li, K.; Lee, P.; Li, S. M. Experimental study of OH-initiated heterogeneous oxidation of organophosphate flame retardants: kinetics, mechanism, and toxicity. *Environ. Sci. Technol.* **2019,** *53*, 14398-14408.
(6) Liu, Y.; Sander, S. P. Rate constant for the OH + CO reaction at low temperatures. *J. Phys. Chem. A* **2015,** *119*, 10060-10066.
(7) Chan, M. N.; Zhang, H.; Goldstein, A. H.; Wilson, K. R. Role of water and phase in the heterogeneous oxidation of solid and aqueous succinic acid aerosol by hydroxyl radicals. *J. Phys. Chem. C* **2014,** *118*, 28978-28992.
(8) Jiang, H.; Jang, M. Dynamic oxidative potential of atmospheric organic aerosol under ambient sunlight. *Environ. Sci. Technol.* **2018**, *52*, 7496-7504.
(9) Liu, Q.; Shahpoury, P.; Liggio, J.; Harner, T.; Li, K.; Lee, P.; Li, S. M. Understanding the key role of atmospheric processing in determining the oxidative potential of airborne engineered nanoparticles. *Environ. Sci. Technol. Lett.* **2020**, *7*, 7-13.
(10) Epstein, S. A.; Blair, S. L.; Nizkorodov, S. A. Direct photolysis of α-pinene ozonolysis secondary organic aerosol: effect on particle mass and peroxide content. *Environ. Sci. Technol.* **2014,** *48*, 11251-11258.
(11) Badali, K.; Zhou, S.; Aljawhary, D.; Antiñolo, M.; Chen, W.; Lok, A.; Mungall, E.; Wong, J.; Zhao, R.; Abbatt, J. Formation of hydroxyl radicals from photolysis of secondary organic aerosol material. *Atmos. Chem. Phys.* **2015**, *15*, 7831.
(12) Zhou, S.; Rivera-Rios, J. C.; Keutsch, F. N.; Abbatt, J. P. Identification of organic hydroperoxides and peroxy acids using atmospheric pressure chemical ionization–tandem mass spectrometry (APCI-MS/MS): application to secondary organic aerosol. *Atmos. Meas. Tech.* **2018**, *11*, 3081.
(13) Krapf, M.; El Haddad, I.; Bruns, E. A.; Molteni, U.; Daellenbach, K. R.; Prévôt, A. S.; Baltensperger, U.; Dommen, J. Labile peroxides in secondary organic aerosol. *Chem* **2016**, *1*, 603-616.
(14) NIST Chemistry WebBook, https://webbook.nist.gov/chemistry/
(15) Volkamer, R.; Klotz, B.; Barnes, I.; Imamura, T.; Wirtz, K.; Washida, N.; Becker, K. H.; Platt, U. OH-initiated oxidation of benzene Part I. phenol formation under atmospheric conditions. *Phys. Chem. Chem. Phys.* **2002,** *4*, 1598-1610.
(16) Atkinson, R.; Arey, J. Atmospheric degradation of volatile organic compounds. *Chem. Rev.* **2003**, *103*, 4605-4638.
(17) Ohta, T.; Ohyama, T. A set of rate constants for the reactions of OH radicals with aromatic hydrocarbons. *Bull. Chem. Soc. Jpn.* **1985**, *58*, 3029-3030.
(18) Liu, Q.; Liggio, J.; Li, K.; Lee, P.; Li, S. M. Understanding the impact of relative humidity and coexisting soluble iron on the OH-initiated heterogeneous oxidation of organophosphate flame retardants. *Environ. Sci. Technol.* **2019,** *53*, 6794-6803.